Macromolecules

pubs.acs.org/Macromolecules Article

Investigating the Kinetics and Structure of Network Formation in Ultraviolet-Photopolymerizable Starch Nanogel Network Hydrogels via Very Small-Angle Neutron Scattering and Small-Amplitude Oscillatory Shear Rheology

Michael J. Majcher, Sebastian Himbert, Francesco Vito, Matthew A. Campea, Ridhdhi Dave, Grethe Vetergaard Jensen, Maikel C. Rheinstadter, Niels M. B. Smeets, and Todd Hoare*

Cite This: https://doi.org/10.1021/acs.macromol.2c00874 Read Online

ACCESS | Metrics & More | Article Recommendations | Supporting Information

ABSTRACT: While photopolymerization has been broadly used to fabricate hydrogels, the kinetics of the structural evolution of such hydrogels during photopolymerization and how the kinetics relate to ultimate hydrogel properties are not well-understood. Herein, small-amplitude oscillatory shear rheology (bulk scale) and time-resolved very small-angle neutron scattering (vSANS, microscale) are used in tandem to investigate the kinetics of the photopolymerization of methacrylated starch building blocks with different concentrations, charges (cationic (+), anionic (−), or neutral (0)), and morphologies (soluble branched starch, starch nanoparticles, or combinations thereof). Starch nanoparticles (SNPs) enabled the fabrication of much denser hydrogels than soluble starch but took longer to gel due to the reduced conformational mobility of the polymerizable methacrylate groups on the SNPs. The addition of charge (cationic or anionic) increases the bulk gelation time while significantly reducing the observed changes in the fluid scale and correlation length, suggesting less covalent crosslinking and inherent SNP deformation during photogelation; indeed, the fluid exponent analysis suggests that charged SNPs deswell upon crosslinking, consistent with the behavior of microgels in colloidal crystals, while uncharged SNPs swell due to competition between inter- and intraparticle crosslinking. The combination of shear rheology and vSANS measurements can thus inform the design of new photopolymerizable hydrogels with targeted comprehensive properties.

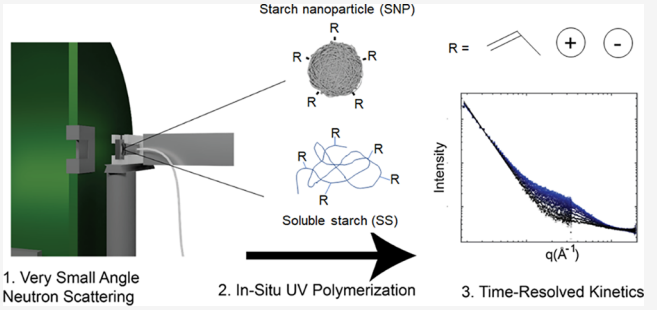

1. INTRODUCTION

Hydrogels have attracted interest for a variety of biomedical applications.[1,2] The high water content and controllable porosity of hydrogels make these materials significantly interesting for use as surface coatings with low protein adsorption,[2,3] biosensor interfaces enabling suppressed biofouling,[4,5] biomedical implants/devices with low inflammatory responses,[6−10] and various bioseparation-based applications.[3,11,12] The underlying micro- and/or nanostructure of the hydrogel determines the efficacy of the hydrogel in each targeted application, whether related to the diffusivity of drugs, cells, or nutrients through the gel (drug delivery/tissue engineering) or the contact angle/degree of hydration of the gel (antifouling). In this context, understanding the porosity and the nature of any inhomogeneities within the gel, as well as how to control such features as a function of the physical morphology and/or chemistry of the hydrogel building blocks, is critical to rationally engineer gels with targeted release kinetics, degradation times, and adsorption properties.

Most conventional hydrogels are fabricated by crosslinking linear polymers or polymerizing monomers and crosslinkers together *in situ*.[13,14] Depending on the nature of the building blocks used (e.g., their relative reaction rates, their propensity to phase-separate, etc.), nano/microscale domains may form that significantly influence hydrogel properties.[15,16] Alternatively, more recent work has investigated the formation of hydrogels from specific building blocks in which well-defined and precrosslinked nano/microgels are subjected to a secondary crosslinking reaction to form a nano/microgel network hydrogel, often referred to as a nanocomposite network hydrogel (NNH).[17] The mechanical, diffusional, and sorption properties of such hydrogels are influenced by both

Received: April 27, 2022
Revised: July 12, 2022

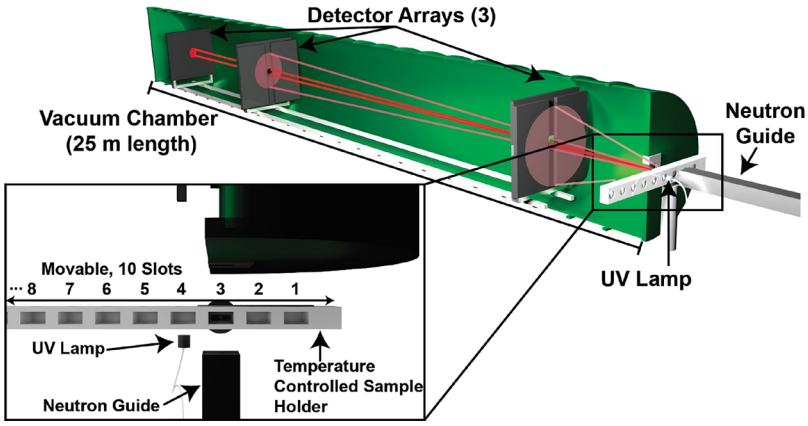

Figure 1. Schematic of the vSANS experimental setup. The instrument consisted of a 45 m-long vacuum tube enclosing a set of three detectors. The sample was loaded into custom-made titanium/quartz sample holders and placed in a temperature-controlled rack fitting up to 9 samples at a time. The UV lamp was placed two slots next to the neutron guide. The sample rack was covered with a black plastic dividing wall for the duration of the experiment to minimize the effect of ambient light.

the size and crosslink density within (intra-) the nano/microscale building blocks as well as the degree and type of crosslink between (inter-) those building blocks, providing multiple levers for controlling hydrogel properties.

Our recent experimental focus in this area lies in using starch nanoparticles (SNPs) as building blocks for fabricating nanoparticle network hydrogels. SNPs are extremely small relative to other nanogel building blocks (20−50 nm on average), are based on a natural, highly cell-compatible, and hydrolytically degradable material (starch), and are available inexpensively at commercial scales, making SNP-based hydrogels relevant to both high-value and commodity (e.g., agriculture or bioremediation) applications. Hydrogels can be formed via facile methacrylation of the SNPs and subsequent thermal or photoinitiated free radical polymerization, with photopolymerization using long-wave (365 nm) or short-wave (264 nm) UV light found to be particularly useful for facile hydrogel formation[18] (Figure 1). SNPs can be crosslinked directly to themselves or by using methacrylated soluble (branched) starch (SS) as a crosslinking agent, offering the potential to form different network morphologies with identical chemistries. Correlating the morphologies of these materials with their properties, in terms of understanding both the final gel properties achieved as well as the structural evolution of such hydrogels as they are formed, is critical for rationally designing hydrogels for targeted applications.

While a variety of methods including dynamic[19] and static light scattering,[20,21] X-ray scattering,[22,23] turbidity/cloud point measurements,[24,25] and advanced electron microscopy methods[26−28] have been used for investigating the internal morphology of hydrogels, small-angle neutron scattering (SANS) is particularly useful given that both the pore size and the dimensions of typical gel inhomogeneities lie in the accessible SANS length scale (1−200 nm).[29−32] SANS is particularly useful for characterizing nanoparticle network hydrogels given that the mesh size of the nano/microgel, the mesh size between the nano/microgels, and the absolute size of the nano/microgels used all lie within the accessible SANS length scale (unlike with other methods).[33] SANS studies on preformed nano/microgel network hydrogels at an equilibrium swelling state have been reported both by our group and others.[34−36] Specific to SNPs and soluble starch, our previous SANS results suggested that SS hydrogels have significantly lower Porod exponents (corresponding to more Gaussian, swollen chains), significantly higher fluid correlation lengths (indicating larger gel mesh sizes), and much larger Lorentzian scales (indicating a significantly more fluid network structure) than SNP-based hydrogels. Furthermore, for SNP-only hydrogels, the degree of interparticle crosslinking was observed to substantially change when either the SNP concentration or the degree of methacrylation was changed (as evidenced by the trends in each of the Lorentzian/fluid-like fluctuation terms).[18] However, the dynamics of the gel formation process and the structural implications of the different building blocks used on those dynamics remain unexplored.

The structural evolution of the hydrogel during gelation has been tracked previously by SANS for other systems containing associative polymers,[37] sticky microgels,[38] proteins,[39] ionic liquids,[40] thermoresponsive polymers,[41] colloidal nanoparticles,[42] and shear-induced gelation,[43] typically using the observed increases in scattering intensity (Porod scattering) over time as a proxy to the rate of the formation of new crosslinks. However, to the best of our knowledge, using SANS to directly track the kinetics of network structural evolution during photopolymerization (for any relevant hydrogel formulation, not just NNHs) has not been reported, in large part due to technical limitations with performing photopolymerization in the neutron beamline and subsequently acquiring relevant kinetic data on the timescale of a typical photopolymerization (often seconds to minutes). In this context, very small-angle neutron scattering (vSANS) offers unique benefits. Built in 2017 and operated by the Center for High Resolution Neutron Scattering (CHRNS) at the National Institute of Standards and Technology (NIST), vSANS enables simultaneous detection of scattered neutrons over a wide q range without requiring moving the detector, enabling much faster data acquisition over the relevant length scales of hydrogels and thus effective tracking of polymerization dynamics.[44]

Herein, we apply the vSANS technique to track the kinetics and structural evolution of the network morphology in hydrogels prepared by photopolymerizing methacrylated soluble starch and/or methacrylated starch nanoparticle building blocks. Specifically, we explore the evolution of the nanostructure of photopolymerizable starch-based hydrogels depending on the concentration of the precursor building

https://doi.org/10.1021/acs.macromol.2c00874
Macromolecules XXXX, XXX, XXX−XXX

blocks, the morphology of the precursor building block (i.e., using either an SNP or soluble branched starch), and the interactions between those building blocks, which we manipulate by functionalizing both types of starch building blocks with cationic or anionic charges as confirmed via proton NMR (^{1}H NMR), elemental analysis (EA), and polyelectrolyte titrations.[45,46] More specifically, by assessing differences in network evolution in hydrogels prepared with different SNP or SS concentrations, different building block morphologies (e.g., soluble starch only, SNPs only, and combinations of SNPs and soluble starch), and varying types of charged building blocks (considering in particular repulsive electrostatic interactions between the SNP building blocks, as is typically used to form colloidal crystals of nanogels),[47] we aim to correlate the physical nature of the building blocks with the structural evolution of the hydrogel during crosslinking. Furthermore, by combining small-amplitude oscillatory shear rheology in which photocrosslinking is conducted directly on the rheometer, the bulk property evolution of the hydrogel over time can be matched with the microstructural evolution identified by vSANS, providing a comprehensive understanding of the network evolution during the photocrosslinking process on multiple length scales.

2. MATERIALS AND METHODS

2.1. Materials. Commercial grade cationic (quaternary ammonium, charge density of 0.34 meq/g) starch nanoparticles, experimental grade EcoSphere starch nanoparticles, and neutral cold water soluble starch (SS) samples were donated by EcoSynthetix, Inc. (Burlington, Ontario, Canada). Pyridine (ACS reagent grade, ≥99%), 1,3-propane sultone (≥99%), methacrylic anhydride (contains 2000 ppm topanol A as an inhibitor, 94%), monochloroacetic acid (ACS reagent grade, ≥99%), and dimethylaminopropylamine (99%) were obtained from Sigma-Aldrich. Sulfuric acid (16 M), methanol (reagent grade), and dimethylsulfoxide (DMSO) were obtained from Fisher Scientific. For all other "wet" steps, Milli-Q deionized water (MQW) with a conductivity between 17 and 18 mΩ was used. For purification of the precursor materials, 3.5−5 kDa cellulose ester dialysis tubing (SpectrumPor) and 0.45 μm PTFE filters (VWR) were used.

2.2. Starch Chemical Modification. *2.2.1. Cationic Functionalization.* Cationic starch nanoparticles with a charge density of 0.34 meq/g were generously gifted to the authors from EcoSynthetix, Inc. for use in this experiment. The substitution of the positive charge was performed by a modified reactive coextrusion process.[48]

2.2.2. Anionic Functionalization. To match the charge density of the commercially supplied cationic SNPs, a protocol for fabricating sulfated (anionic) SNPs was adapted from a previously published method.[49] A pyridinium-methyl-sulfate (Py-Me-S) reagent was first made by adding pure sulfuric acid (95 mL) dropwise to methanol (175 mL) in an ice bath, stirring overnight (~16 h), adding 144 mL of pyridine (1 mol equivalent to sulfuric acid) to the reaction mixture, stirring at 4 °C overnight, washing with toluene three times, and drying the product *in vacuo*. The Py-Me-S reagent was then used to sulfate 20 g batches of SNP or SS using varying molar ratios of Py-Me-S to starch (see Supporting Information, Table S1); to match the charge density of the commercial cationic SNP, a 2.5: 1 molar ratio of Py-Me-S to starch was found to be optimal when the reaction was performed at 60 °C for 3 h in DMSO.

2.2.3. Methacrylation of Starch Precursors. Cationic, anionic, and neutral SNPs and neutral SS samples were subsequently functionalized with methacrylate groups using a previously published protocol.[18] After each modification to the starch chemical structure, samples were purified using 6 different 6 h cycles of dialysis (3.5−5 kDa MWCO) in MQW and lyophilized to form a white fluffy product. Subsequently, methacrylic anhydride (MAAn, 4.56 mL) was used to functionalize 54.3 g of fully dispersed SNPs or dissolved SS in sodium hydroxide (pH 10.4) via a transesterification reaction with primarily C6 hydroxyl groups on the starch backbone, targeting a degree of substitution (DS) of 0.10. Postmethacrylation, all particles were purified via 6 × 6 dialysis cycles (3.5−5 kDa MWCO) in MQW and lyophilized to form the final product. The degree of methacrylation was assessed via ^{1}H nuclear magnetic resonance (NMR, 600 MHz, Bruker) using DMSO-d_6 as the solvent, with the degree of methacrylation calculated by comparing the intensity of the doublets indicative of a methacrylic group (I = 6.2 ppm, C═C) with the intensity of the anomeric carbon (I = 5.4 ppm, 1H) as per previous reports.[18]

2.3. Characterization of Methacrylated Starch Nanoparticles (SNPs) and Soluble Starch (SS). *2.3.1. Elemental Analysis (EA).* Elemental analysis was conducted using an Elementar Unicube using dried SS or SNP samples (2 mg) loaded into 4 × 4 × 11 mm tin boats. Samples were loaded onto an autosampling carousel and run using a combustion tube operating at 900 °C and a reduction tube operating at 799 °C. The samples were standardized using a sulfadimidine standard.

2.3.2. Dynamic Light Scattering (DLS) and Electrophoretic Mobility. The SNP particle size was assessed by dispersing the nanoparticles in Milli-Q water (MQW) at a concentration of 10 mg/mL (1 w/v %), vortexing the sample at 1600 rpm for 1 min, and placing the samples into a low-power bath sonicator for 5−10 min to fully redisperse the SNPs. Vortexed samples were filtered with a 0.45 μm PTFE syringe filter to remove any large aggregates. The particle size was measured on a NanoBrook 90Plus PALS analyzer (Brookhaven, Long Island, NY, USA; temperature = 25 °C), using the refractive index of starch (RI = 1.34) to calculate number-average diameters as required.[50] Electrophoretic mobility measurements were performed by dispersing the SNPs in a 10 mM NaCl solution at a concentration of 10 mg/mL, vortexing, and filtering as described for DLS.

2.3.3. Polyelectrolye Titration. To determine the amount of charge per gram of material (meq/g) on the functionalized SNPs, a particle charge detector (BTG Mutek) was used. Poly(diallyldimethylammonium chloride) (PDADMAC, 0.001 mol/L) was used as the cationic titrant, and poly(vinyl sulfate) (PVSK, 0.001 M) was used as the anionic titrant, both consistent with reported methods.[51,52] The sample was suspended in MQW at concentrations of 10−30 mg/mL in a total volume of 10 mL, after which the oppositely charged titrant was added incrementally to the sample using an autotitrator until the effective surface charge was 0 mV (i.e., all charged groups were titrated).

2.4. Fabrication of Starch Hydrogels. *2.4.1. Homogeneous Gels.* Samples of SS and SNPs, the latter with or without charge functionalization, were suspended at various wt % in MQW, after which 0.15 v/v % 1-[4-(2-hydroxyethoxy)-phenyl]-2-hydroxy-2-methyl-1-propane-1-one (Irgacure 2959) solution was added. The solutions were then placed into silicone molds of the desired size/shape (12.7 mm diameter and 4 mm thick for mechanical testing) and photopolymerized using a UV crosslinking oven (Cure All, 80 mW/cm^2) for 10 min. To minimize the evaporation of water during photocrosslinking, a cooling air jet was applied to control the surrounding temperature. Following irradiation, the hydrogels were parafilmed and left overnight in a crystal dish containing a 200 mL beaker of water (to prevent evaporation/drying) prior to characterization.

2.4.2. Heterogeneous Gels (Mixtures). To assess the network structure evolution as a function of the morphology of the precursor polymers, mixtures containing 2:1, 1:1, and 1:2 ratios of methacrylated SS:SNP were created by dissolving/suspending the required masses of each starch in MQW to achieve a final overall concentration of 10 wt %. These samples were then photocrosslinked as described above to create heterogeneous hydrogels. For all gels, the theoretical degree of substitution of methacrylate groups was 0.10, the final wt % of Irgacure was 0.15 w/v %, and the UV irradiation time was 10 min.

2.5. Small-Amplitude Oscillatory Shear Rheology Measurements. The rheological properties of the photocrosslinked starch

https://doi.org/10.1021/acs.macromol.2c00874
Macromolecules XXXX, XXX, XXX−XXX

hydrogels described above were assessed using a dynamic hybrid rheometer (Discovery HR-2, TA Instruments) maintained at 37 °C with a bottom quartz plate/in-line UV light. For each gel/formulation, three different rheological experiments were performed in sequence on the same initial sample (200 μL total volume): (1) viscosity versus shear rate sweeps of the gel precursor solutions, (2) oscillatory sweeps during *in situ* UV irradiation to measure the gelation time (t_{gel}),[53] and (3) oscillatory sweeps after gelation to assess the mechanics of the fully formed network (via the plateaus in the G' and G'' profiles as a function of oscillation frequency).

2.5.1. Precursor Solution Viscosity. To assess the viscosity of the precursor starch solutions/suspensions, a viscosity versus shear rate test was performed using a 20 mm aluminum top plate, a 20 mm quartz bottom plate, a 0.5 mm (500 μm) parallel plate gap, shear rates from 0.1 to 100 s^{-1} (forward direction only), 5 points per decade, an average sampling time of 30 s, and an equilibration time of 5 s.

2.5.2. Oscillation Tests for Gelation Time and Postgelation Mechanics. Directly after performing the viscosity flow tests on the precursor solutions, a UV accessory was used to determine the gelation time (t_{gel}), defined as the point of inflection in the G'/G'' curve that represents the onset of significant elasticity in the network during the photopolymerization process. A "fast oscillation sweep" experiment was performed by applying a 1% strain at a frequency of 1 Hz for 30 s, after which UV light (80 mW/cm^2, 365 nm wavelength) was used to *in situ* photocrosslink the precursor starch solutions/suspensions on the rheology platform through a quartz window for a total of 10 min (600 s);[54] the storage modulus (G') and loss modulus (G'') were measured every 30 s over the entire 10 min irradiation window. Following gelation, the sample was left for 10 min to ensure that the crosslinking was complete, after which a strain sweep was first conducted to confirm operation within the linear viscoelastic region (LVE) followed by a frequency sweep (at a 1% strain) from 0.1 to 100 rad/s to measure G' and G'' for the final hydrogel.

2.6. Very Small-Angle Neutron Scattering (vSANS). *2.6.1. Experimental Procedure.* Very small-angle neutron scattering (vSANS) measurements were performed on neutron guide B3 at the NIST Center for Neutron Research (NCNR) in Gaithersburg, MD, USA.[55] The instrument setup is shown in Figure 1. All gel precursor solutions were prepared using starch nanoparticle concentrations of 10−35 wt % and soluble starch concentrations of 5−10 wt % (consistent with the gelation work performed above) using D_2O as the solvent. Precursor solutions/suspensions were loaded into the NCNR's custom-made titanium sample chamber with quartz windows on either side (diameter of 19 mm and path length of 2 mm). The chamber was placed in a temperature-controlled rack in front of a 25 m-long evacuated tube enclosing a set of two helium-3 detectors positioned 4.12 and 19.12 m away from the sample and a third scintillator-CCD detector positioned 23.02 m away from the sample. Note that while the experiment was performed during the instrument's commission period in which the low-q detector (23.02 m) was not operational, the accessible q range (2×10^{-3} to 1 $Å^{-1}$) was still directly relevant to the length scales being probed to track photogelation. The instrument was operated in its white beam configuration to maximize the neutron flux, resulting in a non-Gaussian wavelength spread of 40%; to compensate for that, the model was smeared accordingly as further described in Section 2.6.2.

A Prizmatix ultrahigh-power light guide-coupled UV LED (UHP-F-5-365, 365 nm) was mounted parallel to the neutron guide such that the light illuminated the sample two slots next to its position in the neutron beam. Hereafter, the sample position used for the SANS measurement will be referred as the SANS slot and the position for UV exposure as the UV slot. The entire sample stage was covered with a black plastic dividing wall to prevent ambient light from accessing the sample. Each sample was measured according to the following protocol: (1) take one SANS measurement; (2) move the sample to the UV slot; (3) expose the sample to UV light for 3 s; (4) move the sample to the SANS slot; (5) take one SANS measurement; (6) move the sample back to the UV slot and re-expose to UV light for 3 s; (7) repeat 10 times to collect a set of 11 measurements for each sample tracking the structural evolution in the hydrogel during stepwise UV exposure (total power of 6 W, 5 mm LLG core). Note that the Prizmatix UV light guide has a much higher power (up to 70 W/cm^2) than the UV light used for the rheology work (80 mW/cm^2) in order to achieve a maximum run time of 10 min per sample with 10 measurements for the kinetic profile, resulting in a total exposure time of 30 s; as such, while the scaled kinetics of the structural evolution are expected to be comparable, the gelation timescales for the two methods are not directly comparable.

2.6.2. Fitting Parameters and Modeling. Scattering profiles were fit using Shibayama's approach of combining an Ornstein−Zernicke scattering term with a Lorentzian term to account for the presence of domains (here, the denser SNPs relative to the less dense inter-SNP region) as well as the dynamics of the gel network (eq 1):[56]

$$I(Q) = \frac{s_{\text{Porod}}}{Q^n} + \frac{s_{oz}}{1 + (Q\xi)^m} + b \tag{1}$$

Equation 1 is an empirical model and was developed by Hammouda and coworkers at NIST to analyze the scattering spectra of polymer solutions and hydrogels using the $I(q)$ scattering intensity and the scattering vector (q).[57] The measured spectrum only shows the tail of a low-Q feature arising from large-scale (small-Q) clusters. The accessible Q range is insufficient to determine exact particle sizes and is thus approximated by a Porod term (first term in eq 1). The second term has the shape of an Ornstein−Zernike Lorentzian and describes scattering from the polymer chains. In eq 1, s_{Porod} and s_{oz} measure the scale/weightings of the Porod and Ornstein−Zernike Lorentzian functions, respectively, n is the Porod exponent describing clustering and swelling within a network (dominating the low-q regime of the SANS profile),[57,58] ξ is the spatial correlation length of the hydrogel network and increases with progressive crosslinking, m is the Lorentzian exponent corresponding to polymer−solvent interactions, and b denotes the q-independent background resulting from incoherent neutron scattering.[30,59]

Using the instrument in its white beam configuration has the consequence of measuring a spectrum that is convoluted with the beam's own wavelength distribution, the correction for which was performed by convoluting eq 1 with the white beam spectrum provided by NIST. The model parameters were determined for each sample and plotted against the UV exposure time to assess the structural evolution in the hydrogels over the time course of photocrosslinking. Exposure time-dependent trends observed with the correlation length ξ and the scale s_{oz} of the Ornstein−Zernike Lorentzian were fit using a stretched exponential function (eqs 2 and 3):

$$\xi(t) = e^{-\left(\frac{1}{\tau_\xi}t\right)^{\beta_\xi}} \tag{2}$$

$$s_{oz}(t) = e^{-\left(\frac{1}{\tau_S}t\right)^{\beta_S}} \tag{3}$$

Here, τ_ξ and τ_S are the time constants of the dynamic processes (i.e., the photocrosslinking reaction), and β_ξ and β_S denote the stretch that models relaxation processes in glass-like liquids ($\beta = 1$ denotes an isotropic relaxation, while $0 < \beta_\xi$ and $\beta_S < 1$ indicate an anisotropic relaxation and an anomalous diffusion process[60−62]). Work by de Gennes[63] supports the idea that the correlation length ($\xi(t)$) in homogeneous gels should be equal to or less than size of the average mesh size and should not differ significantly from the correlation length of a polymer solution at the same concentration.[64]

Fits were performed using MATLAB, and the spec1d library provided by the Institute Laue−Langevin, Grenoble, France by computing the least-squares fit for a given function and dataset using the Levenberg−Marquardt minimization algorithm.[65,66] For fitting the Porod model, initial guesses for the parameters were provided to the algorithm. In the first step, the parameter space was explored, and initial guesses were optimized to ensure a convergence of the fit for all datasets over a range of compositions and time points. These optimized values were subsequently used for the initial guesses in fitting all datasets: $s_{oz} = 1.611 \times 10^{-6}$, $s_{oz} = 2.38 \times 10^{-5}$, $n = 2.5$, $b = 0.2$, $\xi = 27.31$, and $m = 3.17$.

https://doi.org/10.1021/acs.macromol.2c00874
Macromolecules XXXX, XXX, XXX−XXX

Table 1. Effective Diameter (by Intensity or Number Weighting), Electrophoretic Mobility, and Surface Charge Density of Native and Functionalized Starch Nanoparticle (SNPs) Used for Hydrogel Fabrication

starch type	effective diameter by intensity (nm)[a]	effective diameter by number (nm)[a]	electrophoretic mobility ($\times 10^{-8}$ $m^2/(V\ s)$)[b]	surface charge density (meq/g)[c]	degree of functional (charged) group substitution[d]	degree of methacrylation[e]
(0)SNP	132 ± 2	28 ± 2	+0.03 ± 0.15	0.00		0.10
(−)SNP	175 ± 13	25 ± 7	−0.79 ± 0.06	−0.41	0.12	0.09
(+)SNP	264 ± 14	19 ± 12	+0.45 ± 0.05	+0.35	0.05	0.11

[a]From dynamic light scattering. [b]From phase analysis light scattering zeta potential measurements. [c]From polyelectrolyte charge titration. [d]From elemental analysis. [e]From ^{1}H NMR.

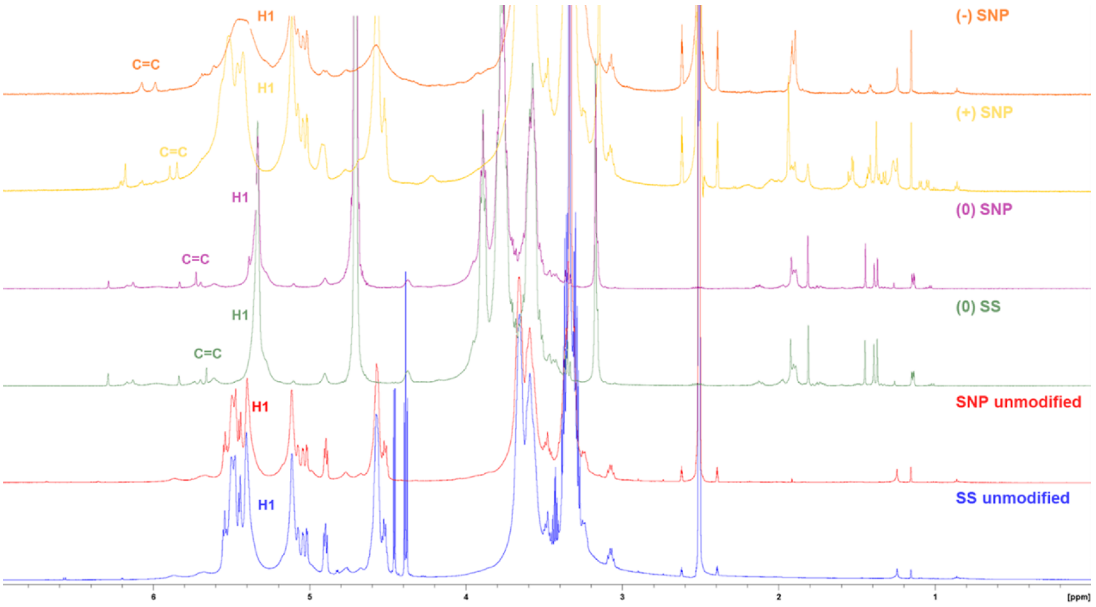

Figure 2. ^{1}H NMR spectra of methacrylated neutral and charged soluble starch (SS) and starch nanoparticles (SNP) relative to the nonmethacrylated precursor polymers. The area under the doublets, indicative of a methacrylic group (I = 6.2 ppm, C═C), was compared to the anomeric carbon (I = 5.4 ppm, 1H) intensity to calculate the degree of substitution (DS).

The least-squares fit was performed twice, with the results from the first fit used as starting parameters for the second fit.

3. RESULTS AND DISCUSSION

3.1. Characterization of Starch Precursors. Dynamic light scattering (DLS) was used to determine the particle size of the starch nanoparticles before and after chemical modification. All modified SNPs have intensity-based particle sizes varying between 130 and 260 nm but a number-based particle size consistently lying in the range of 19−28 nm (Table 1 (column a)). These results are consistent with previous work[18] and suggest that SNP suspensions consist of very small nanogel-based gel building blocks that undergo a minimal degree of self-aggregation when suspended in water. Electrophoretic mobility measurements on the SNPs (Table 1 (column b)) show that the neutral (base) SNP has a net zero surface charge, while the anionic SNPs have an electrophoretic mobility of -0.79×10^{-8} $m^2/(V\ s)$, and the cationic SNPs show an electrophoretic mobility of $+0.45 \times 10^{-8}$ $m^2/(V\ s)$, confirming the success of the functionalization protocols for introducing negative and positive charges on the respective SNPs. Polyelectrolyte charge titration (using anionic PVSK as the titrant for the cationic SNPs and cationic PDADMAC as the titrant for the anionic SNPs) further confirms these results (Table 1 (column c)), with the charge density of both cationic and anionic SNPs lying in the range of |0.35−0.41| meq/g at the optimal (−)SNP sample identified to match the charge density of the industrially sourced (+)SNP sample (see Supporting Information, Table S1 for details on this optimization process). Elemental analysis further confirms this result, with cationic functionalized SNPs showing an increase in % N from 0.16 to 0.42 atom % (Supporting Information, Figure S2A), while the % S increases in a systematic manner as the ratio of pyridinium methyl sulfate to starch is increased from 1:0.05 (0.07 atom % S) to 1:10 (5.1 atom % S) (Supporting Information, Figure S2B). Subsequent methacrylation resulted in no significant changes in either the number-average diameter or the electrophoretic mobility of the SNPs (p > 0.05 in all pairwise comparisons versus the nonmethacrylated precursor material), with the degree of methacrylation (DS) based on NMR analysis being 0.10 ± 0.01 for all SNPs (DS = 0.09−0.11, Table 1 (column e) and Figure 2) and the soluble starch (SS) sample (DS = 0.10).

Note that the anionic (sulfated) SNPs showed a higher absolute electrophoretic mobility value (Table 1) and a higher S mol % (Supporting Information, Figure S2) than the cationic SNPs despite the very similar polyelectrolyte charge titration results observed for the anionic and cationic samples. We hypothesize that the sulfation chemistry may be more effective at internally functionalizing the SNPs relative to the cationic chemistry used, recognizing that electrophoretic mobility measurements in soft nanoparticles like SNPs also measure some internally contained charges. However, we believe the comparison of the effect of charge on gelation to be best

https://doi.org/10.1021/acs.macromol.2c00874
Macromolecules XXXX, XXX, XXX−XXX

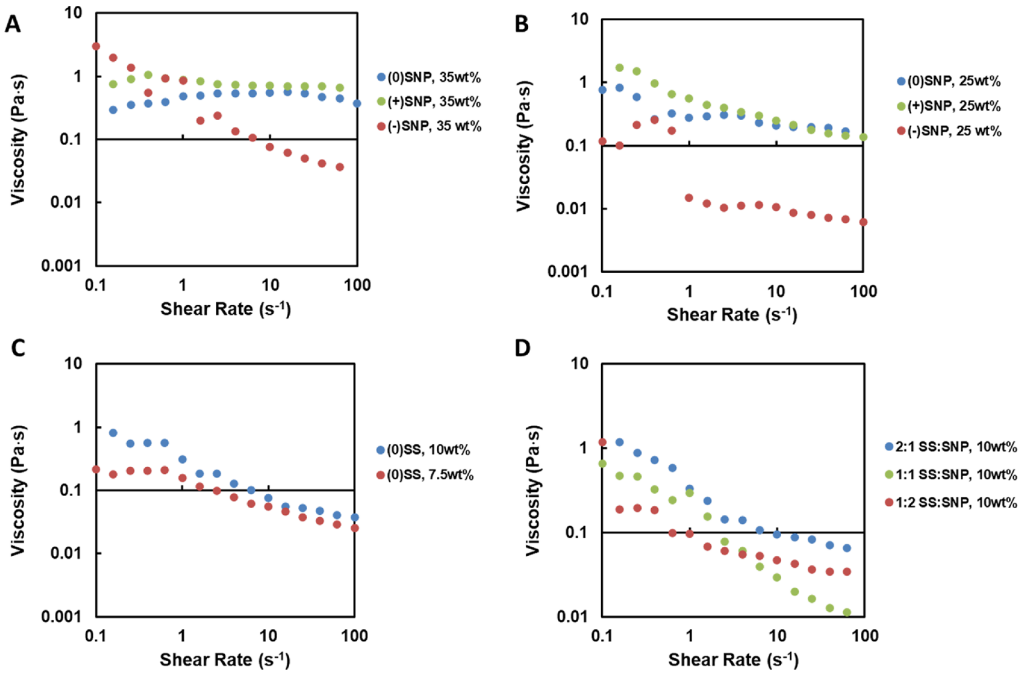

Figure 3. Viscosity versus shear rate flow sweeps to determine the relationship between shear and viscosity for (A) 35 wt % homogeneous gels (SNP building blocks), (B) 25 wt % homogeneous gels (SNP building blocks), (C) SS-based homogeneous gels at different concentrations (10 and 7.5 wt %), and (D) 10 wt % heterogeneous gels (mixtures of SS and SNP building blocks).

conducted by matching the surface charge density as measured by the polyelectrolyte charge titration data, for which the charge density of the cationic and anionic SNPs matches, rather than the electrophoretic mobility values. As such, all precursor starches have essentially the same degree of methacrylation (0.10 ± 0.01), and all charged SNPs have equivalent surface charge densities (∼|0.40| meq/g), allowing direct comparisons to be made between the hydrogels formed from the different precursors.

3.2. Rheology. *3.2.1. Pregelation Viscosity.* To assess the impacts of the concentration, morphology, and charge of the starch gel precursors on the initial viscosities of the pregel solutions/suspensions, viscosity versus shear rate tests were performed (Figure 3); the shear thinning viscosity data for each sample extracted only at shear rates of 0.1, 1, 10, and 100 1/s are available in Supporting Information, Figure S3 to enable more direct comparisons between the samples. Note that the concentration ranges tested (25−35 wt % for SNPs, 7.5−10 wt % for SS) were chosen based on the upper range of the solubility of the SS as well as the concentration of the more compact SNPs previously identified to form hydrogels rather than simply viscous solutions following photocrosslinking.[18]

The SS-only and SNP-SS mixture gel precursor solutions are shear thinning across all weight percentages tested, consistent with another waxy starch study.[67] However, SNP-only samples show consistently lower viscosities and significantly less shear thinning behavior than SS samples, with the 35 wt % (0)SNP and (+)SNP precursors in particular exhibiting essentially no significant shear thinning over the shear rate range studied. This result is consistent with the higher molecular weight, degree of hydration, and potential for intermolecular entanglements observed with the branched soluble SS compared to the crosslinked compact SNPs. Correspondingly, increasing the concentration of either SS or SNPs (comparing Figure 3A,B for SNPs or Figure 3C for SS) also results in increased viscosities. Introducing a cationic or anionic charge increases the precursor suspension viscosity at low shear, consistent with electrostatic repulsion between the precursor materials in solution; however, the charged SNPs also shear thin more than the neutral SNPs as the shear forces can better compete with the electrostatic repulsive forces present, particularly for the (−)SNP samples that appear to be similarly shear thinning to the SS samples. With respect to the mixtures of SS and SNPs (Figure 3D), as more SS is included in the system, a higher observed viscosity at low shear rates and more shear thinning of the sample at higher shear rates are observed, consistent with increased chain entanglement as more SS is added to the less conformationally mobile SNPs in the precursor starch mixture. As such, both the charge and the morphology of the starch precursor(s) used significantly alter the interparticle/interchain interactions in solution prior to gelation.

3.2.2. In Situ Gelation Kinetics. To assess the effects of the starch concentration, morphology, and charge on the photocrosslinking of the methacrylated starches to form hydrogels, an *in situ* photocrosslinking experiment was conducted using the UV accessory on the rheometer to determine the time of gelation (t_{gel}). The time of gelation (t_{gel}) was defined at the time point corresponding to the inflection point in the G' and G'' plots vs time reflecting the onset of elastic-like responses in the hydrogel; note that this metric was chosen instead of the more conventional $G'/G'' = 1$ convention since some of the precursor polymer samples (particularly higher concentration SS samples) were already highly viscous and showed $G'/G'' > 1$ even before photocrosslinking, making that metric incompatible with our system (Supporting Information, Figure S4). The resulting gelation times measured for each sample are shown in Table 2.

In all cases, increasing the concentration of any SS or SNP precursor accelerates gelation, while functionalizing the SNPs with charge significantly slows gelation, with (+)SNP and (−)SNP both observed to gel slower than the neutral SNPs at

https://doi.org/10.1021/acs.macromol.2c00874
Macromolecules XXXX, XXX, XXX−XXX

Table 2. Gelation Time (t_{gel}) for Methacrylated Starch Photogelation as a Function of Starch Concentration, Morphology (SS or SNP), and Charge

sample	gel type	wt %	t_{gel}, s
(0)SNP	homogeneous	35	32
(0)SNP	homogeneous	25	56
(+)SNP	homogeneous	35	46
(+)SNP	homogeneous	25	88
(−)SNP	homogeneous	35	50
(−)SNP	homogeneous	25	99
(0)SS	homogeneous	10	20
(0)SS	homogeneous	7.5	39
2:1 SS:SNP	heterogeneous	10	41
1:1 SS:SNP	heterogeneous	10	57
1:2 SS:SNP	heterogeneous	10	92

both concentrations tested. This trend is consistent with the interparticle (repulsive) particle interactions in the pregel suspension restricting the proximity of the polymerizable methacrylate groups on the SNPs and thus slowing photocrosslinking. For mixed precursor hydrogels, the gelation time varies with the proportion of the more flexible and sterically accessible SS component included in the mixture, with higher SS contents resulting in faster gelation times as expected based on the SS-only and SNP-only gelation times measured.

3.2.3. Postgelation Mechanical Properties. Following gelation, a full frequency sweep was conducted to assess the mechanical properties of the resulting hydrogels, the results of which are shown in Figure 4.

The use of SNPs results in the formation of significantly stiffer hydrogels, consistent with the much higher concentration of starch that can be used to prepare the hydrogels as a result of the nanoparticle rather than the soluble/branched structure of the starting material coupled with the already internally crosslinked internal structure of the SNPs. Charged SNP-based hydrogels are consistently stiffer than their neutral counterparts at the same weight fraction, suggesting that repulsive interactions between the charged SNPs enhance the mechanics of the resulting hydrogel. In terms of the morphology of the building blocks, a 1:1 mixture of SS and SNP results in the lowest measured modulus value, with both 2:1 and 1:2 SS:SNP ratios yielding stiffer hydrogels. We hypothesize this result corresponds to the combined effects of more SNPs providing enhanced mechanical strength based on the internally crosslinked structure of the SNP (a dominant effect at the 1:2 SS:SNP ratio) and the presence of more SS providing more effective interparticle crosslinking given that the methacrylate groups are less sterically hindered to polymerization than they are on the more rigid SNPs (a dominant effect at the 2:1 SS:SNP ratio).

3.3. Very Small-Angle Neutron Scattering. To track the structural evolution of the hydrogels during photopolymerization as a function of the charge and morphology of the starting materials, the unique combination of the high neutron flux and the simultaneous measurement of a wide q range offered by the vSANS instrument is leveraged to probe the intermediate gel nanostructures in real time during the photopolymerization process. Figure 5 shows a representative sample (for the 35 wt % neutral SNP gel) of the kinetic data acquired.

The nonlinear least-squares fit of the data enables the extraction of five fitting parameters. The two scale parameters (i.e., the Porod scale s_p and the fluid scale s_{oz}) correspond to the relative weightings of the Porod and Ornstein−Zernike functions required to fit the data, with the Porod term dominating at low q and a Lorentzian term dominating at high q. Given that the major differences in the SANS curves (such as Figure 5) were observed in the mid to high q range, the fluid scale s_{oz} is particularly relevant to this analysis, consistent with the Lorentzian term corresponding to the dynamics of the hydrogel network; more specifically, changes in the fluid scale can be used to track changes from more fluid-like systems

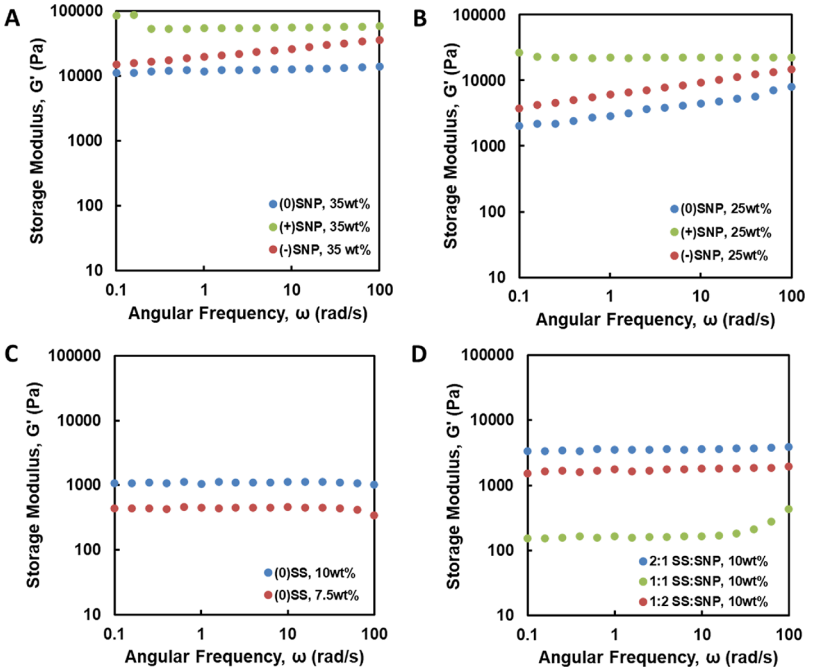

Figure 4. Postgelation mechanical properties for SS- and/or SNP-based hydrogel systems fabricated at concentrations of (A) 35 (SNP only), (B) 25 (SNP only), and (C) 10 and 7.5 (SS only) and (D) 10% (mixed SS/SNP).

https://doi.org/10.1021/acs.macromol.2c00874
Macromolecules XXXX, XXX, XXX−XXX

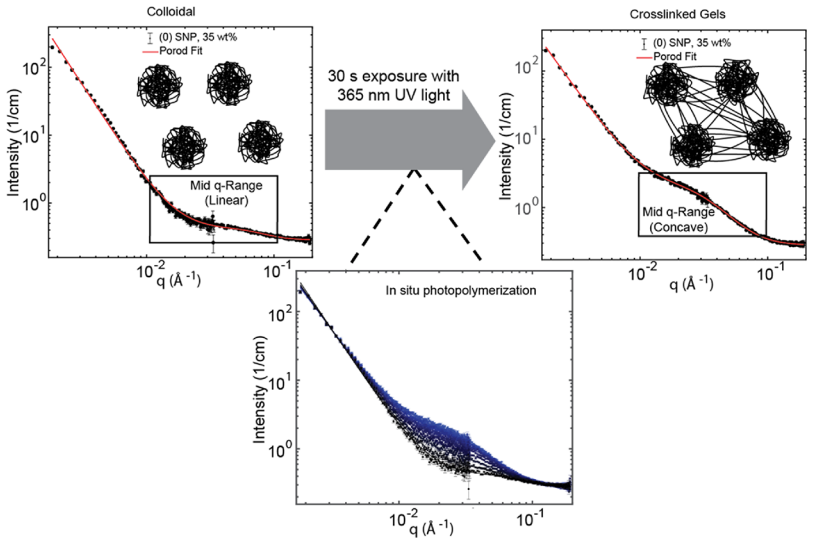

Figure 5. Schematic showing the evolution of network formation from concentrated SNP colloids to crosslinked SNP gels over a 30 s exposure time to 365 nm light.

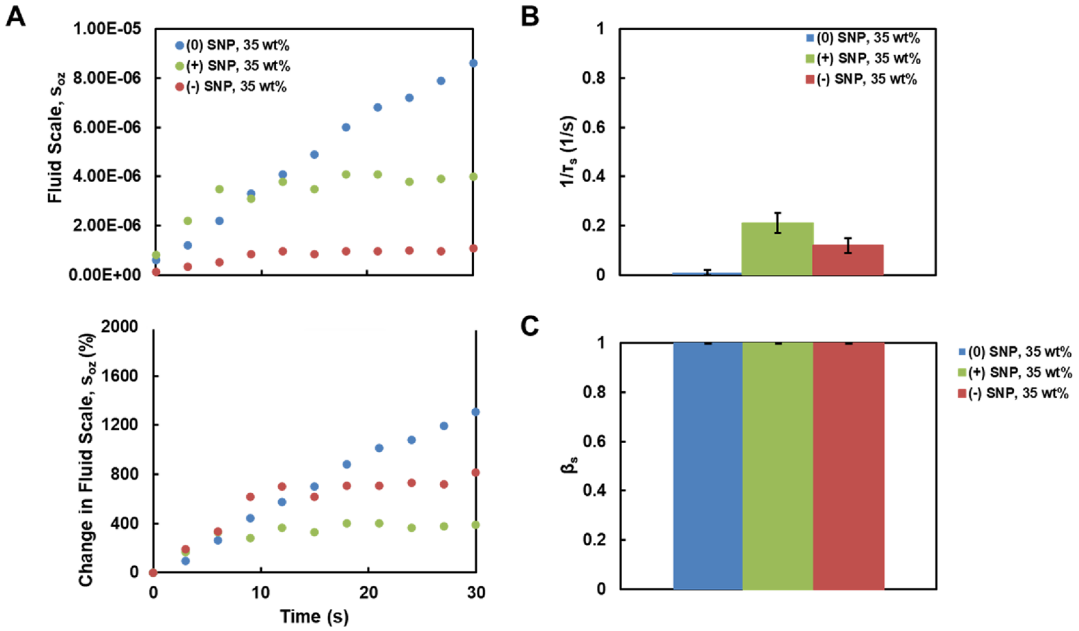

Figure 6. Measured changes in the fluid scale over 30 s of UV exposure ((A) top = absolute values, bottom = percent changes over the irradiation time) and best-fit time constant ($1/\tau_S$, B) and stretch parameter (β_S, C) for 35 wt % homogeneous SNP hydrogels formed in the beamline (error bars represent ± standard deviation).

(pregelation, low fluid scale) to less fluid-like/more solid-like systems (postgelation, high fluid scale), consistent with the progression of gelation. The two exponents (i.e., the Porod exponent n and the Lorentzian exponent m) also give key insight into the physics of the system. Porod exponents of $n \approx 2$ indicate that the system is composed of Gaussian swollen chains, while a value of 3 or higher indicates that there is a clustering of mass within the system, the latter consistent with denser SNPs crosslinked together into a network by less dense crosslinking domains. A Lorentzian exponent of $m \leq 2$ indicates that the polymer chains are behaving as if they are in a good solvent, while $m > 2$ indicates reduced polymer−solvent interactions. Finally, the correlation length ξ gives insight into the changing distance between inhomogeneities in the system over time based on the changing position of the Lorentzian term over the course of the experiment, herein indicative of changes in the interparticle spacing between the denser SNP domains as crosslinking progresses.

Given that the small-angle oscillatory shear rheology measurements presented above track the evolution of gelation on the bulk scale, we selected the fluid scale as the most appropriate parameter to track from the vSANS analysis since it provides a microscale representation of gelation that can be correlated to the bulk shear rheology measurements. The kinetic trends in the fluid scale were extracted from each *in situ* photopolymerization experiment and fit to eq 3. The corresponding evolution of the correlation length is shown in Supporting Information, Figures S5, S7, S9, and S11 (including the best-fit terms to eq 2), while the evolution of the Porod and Lorentzian (fluid) exponents over time is shown in

https://doi.org/10.1021/acs.macromol.2c00874
Macromolecules XXXX, XXX, XXX−XXX

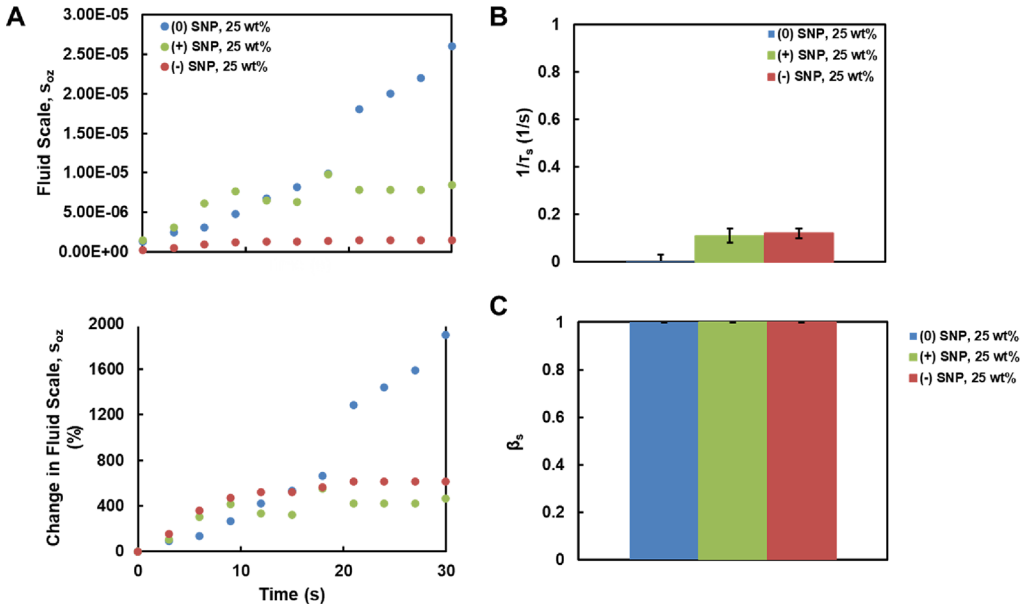

Figure 7. Measured changes in the fluid scale over 30 s of UV exposure ((A) top = absolute values, bottom = percent changes over the irradiation time) and best-fit time constant ($1/\tau_S$, B) and stretch parameter (β_S, C) for 25 wt % homogeneous SNP hydrogels formed in the beamline (error bars represent ± standard deviation).

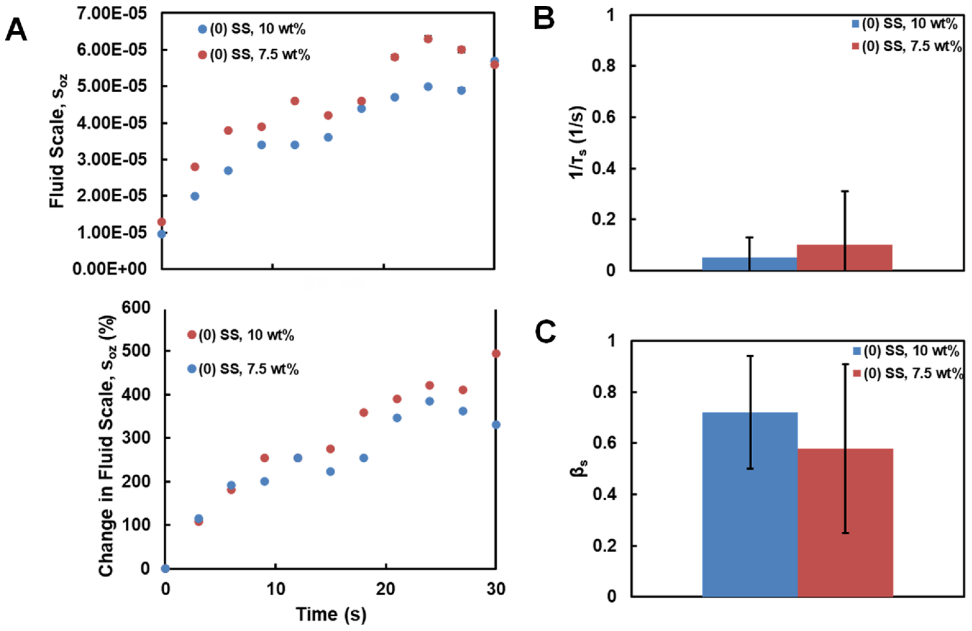

Figure 8. Measured changes in the fluid scale over 30 s of UV exposure ((A) top = absolute values, bottom = percent changes over the irradiation time) and best-fit time constant ($1/\tau_S$, B) and stretch parameter (β_S, C) for homogeneous SS hydrogels formed in the beamline (error bars represent ± standard deviation).

Supporting Information, Figures S6, S8, S10, and S12. A full summary of the fitting parameters used to fit the scattering data for all samples tested can also be found in the Supporting Information, Tables S2−S12.

3.3.1. Effect of the Starch Precursor Concentration. Figure 6A (for 35 wt % SNP gels), Figure 7A (for 25 wt % SNP gels), and Figure 8A and 8B (for SS gels) show the evolution of the fluid scale expressed as both an absolute value and a percentage change over the 30 s duration of the UV photoirradiation period; correspondingly, Figure 6B (35 wt % SNPs), Figure 7B (25 wt % SNPs), and Figure 8C (SS) show the comparative gelation rates as defined by the inverse of the exponential best-fit time constant ($1/\tau$, where a larger value for $1/\tau$ indicates a slower gelation time and a longer t_{gel}), while Figure 6C (35 wt % SNPs), Figure 7C (25 wt % SNPs), and Figure 8C (SS) show the stretch parameter β_S required for the best fit of the fluid scale over time (see eq 3 for definitions of these terms). Refer to Supporting Information, Figures S5 (35 wt % SNPs), S7 (25 wt % SNPs), and S9 (SS) for the corresponding figures showing the evolution of the fluid correlation length.

Nearly linear correlations were observed between the fluid scale and the UV exposure time for the (0)SNP gels at both concentrations tested (Figures 6A and 7A), and no significant characteristic timescale (i.e., very slow dynamics) was observed

https://doi.org/10.1021/acs.macromol.2c00874
Macromolecules XXXX, XXX, XXX−XXX

related to the exponential fit of the kinetics data over the timescale analyzed; zero lies within the experimental error of each $1/\tau$ value measured (Figures 6B and 7B), and the stretch parameter remains at ∼1, suggestive of an isotropic relaxation process (Figures 6C and 7C). By comparing the percentage changes in the Porod exponent (n) and the fluid/Lorentzian exponent (m) for 35 and 25 wt % homogeneous SNP hydrogels, additional insight can be gained into the effect of photocrosslinking on the internal structure of the uncharged SNP homogeneous gels. The Porod exponents (Supporting Information, Figures S6A and S8A) remain just below 3 for both (0)SNP gels tested and do not significantly change throughout the entire photopolymerization process, suggesting that the SNPs remain distinct nanoparticles (and as such localized mass scattering units) even after gelation. However, the fluid exponents (Supporting Information, Figures S6B and S8B) decrease by ∼40% for (0)SNP 35 wt % and ∼32% for (0)SNP 25 wt %, suggesting that crosslinking improves the solubilization of the polymer chains comprising the SNPs. We hypothesize that this observation is related to the pulling on individual starch chains as polymerization proceeds, competing with the internal crosslinking within the SNPs and thus extending the starch chains within the SNPs into a less collapsed state. This interpretation is also supported by the continual increases in the correlation length during photopolymerization (Supporting Information, Figures S5A and S7A), consistent with the interface of the SNPs becoming more hydrated to increase the distance between the dense polymer-rich domains remaining inside each SNP.

The same general trend of increasing fluid scales and correlation lengths can be seen for the (uncharged) SS-based hydrogels in Figure 8; however, based on a comparison of the y-axis ranges in Figures 6A and 7A (SNP gels, maximum y-value of 1×10^{-5}) and Figure 8A (SS gels, maximum y-value of 7×10^{-5}), the fluid scale of SS samples is much higher than that of the SNP gels despite the much lower mass concentration of starch present in SS-based hydrogels. In addition, the percentage change in the fluid scale observed over the course of the gelation process is significantly smaller with SS-based hydrogels relative to that observed with SNP-based hydrogels. This result is consistent with our previous work that indicated a significant molecular weight difference between SS (∼5,000,000 g/mol) and SNPs (∼250,000−500,000 g/mol, both based on linear pullulan standards);[18,68] coupled with the similar initial viscosities of the SS and SNP starting solutions (Figure 3) but the significantly lower modulus achieved in the SS-based hydrogels (Figure 4), gelation in the SS-based systems appears to result in a lower net change in the elastic properties of the system as compared with SNP-based hydrogels. The more inverse exponential-like shape of the SS-based hydrogel gelation is also consistent with the bulk gelation kinetics data from the small-amplitude oscillatory shear rheology experiments (Table 2), which indicated that SS-based hydrogels gel faster (and thus reach their equilibrium crosslink density over a shorter period of time) compared to SNP-based hydrogels. Thus, although the absolute magnitudes of the gelation times vary based on the different light source powers observed, bulk rheological data and microscopic structural parameter tracking via vSANS result in similar trends. Interestingly, despite the (0)SNP 35 wt % gel forming faster than the (0)SS 7.5 wt % gel based on bulk gelation measurements (32 s versus 39 s, respectively, Table 2), the (0)SS 7.5 wt % gel achieves a plateau in the fluid scale after ∼20 s, while the fluid scale in the (0)SNP 35 wt % gel keeps increasing in a nearly linear fashion over the full 30 s irradiation period. This result implies that the SNP-based gels undergo significantly more internal rearrangement following the observation of macroscopic gelation relative to SS-based gels.

The Porod and fluid exponent trends (Supporting Information, Figure S10) are also consistent with the different dynamics of SS versus SNP polymerization. The Porod exponent shows a significant decrease (15−18% depending on SS concentration) while the fluid exponent remains essentially unchanged during photopolymerization for both SS-based hydrogels tested. We interpret this result as crosslinking having a minimal effect on the local chain hydration with SS-based hydrogels but reducing the degree of mass clustering as semicollapsed starch chains are stretched by the crosslinking process. The concurrent significant increase observed in the correlation length is also consistent with fewer mass-clustered domains being observed as the crosslinking proceeds, unlike in the SNP-based gels in which the internally crosslinked SNP retains locally higher mass concentration domains throughout photopolymerization.

3.3.2. Effect of the Charge. As with the neutral (0)SNP-based hydrogels, hydrogels prepared with (−)SNP and (+)SNP also showed lower changes in the fluid scale over the gelation time if the concentration of the SNP building block is increased (Figures 6A and 7A). However, while the fluid scale of the (0)SNP gels showed a nearly linear correlation with the polymerization time, hydrogels formed based on (+)SNP and (−)SNP show very different fluid scale trends over time. Both anionic and cationic SNP gels undergo only a small increase in the fluid scale in the first 10−12 s of irradiation followed by a plateau over the rest of the experiment. Comparing the effect of the charge, at each concentration tested, (0)SNP shows the largest overall change in the fluid scale (Figures 6A and 7A), the lowest characteristic timescale ($1/\tau = 0.01 \pm 0.01$ s^{-1} at 35% and 0.00 ± 0.03 s^{-1} at 25 wt %) (Figures 6B and 7B), and the shortest bulk gelation time (32 s at 35 wt % and 56 s at 25 wt %) (Table 2), while (+)SNP shows intermediate overall changes in the fluid scale (Figures 6A and 7A), the characteristic timescale ($1/\tau = 0.21 \pm 0.04$ s^{-1} at 35 wt % and 0.11 ± 0.03 s^{-1} at 25 wt %) (Figure 6A and 7A), and the bulk gelation time (46 s at 35 wt % and 88 s at 25 wt %) (Table 2), and (−)SNP shows the smallest overall change in the fluid scale (Figures 6A and 7A), the highest characteristic timescale ($1/\tau = 0.12 \pm 0.03$ s^{-1} at 35 wt % and 0.12 ± 0.02 s^{-1} at 25 wt %) (Figures 6B and 7B), and the slowest bulk gelation time (50 s at 35% and 99 s at 25%) (Table 2). All uncertainties were determined from the least-squares fit of eq 2. Interestingly, the stretch parameter remains equal to 1 (corresponding to isotropic relaxation) irrespective of the SNP charge (Figures 6C and 7C). Combining these observations together, we hypothesize that the significantly lower changes in the fluid scale observed for the charged SNP-based hydrogels are related to the high interparticle repulsion present between the charged SNPs due to charge−charge interactions, which both limits the closeness of approach of the SNPs to facilitate covalent crosslinking and also provides a colloidal crystal-like electrostatic gelation effect when the SNPs are brought sufficiently close together by the formation of covalent crosslinks. Thus, while the fluid scale results suggest that significantly less covalent photogelation occurs in the charged SNP-based hydrogels, the inherent high degree of

https://doi.org/10.1021/acs.macromol.2c00874
Macromolecules XXXX, XXX, XXX−XXX

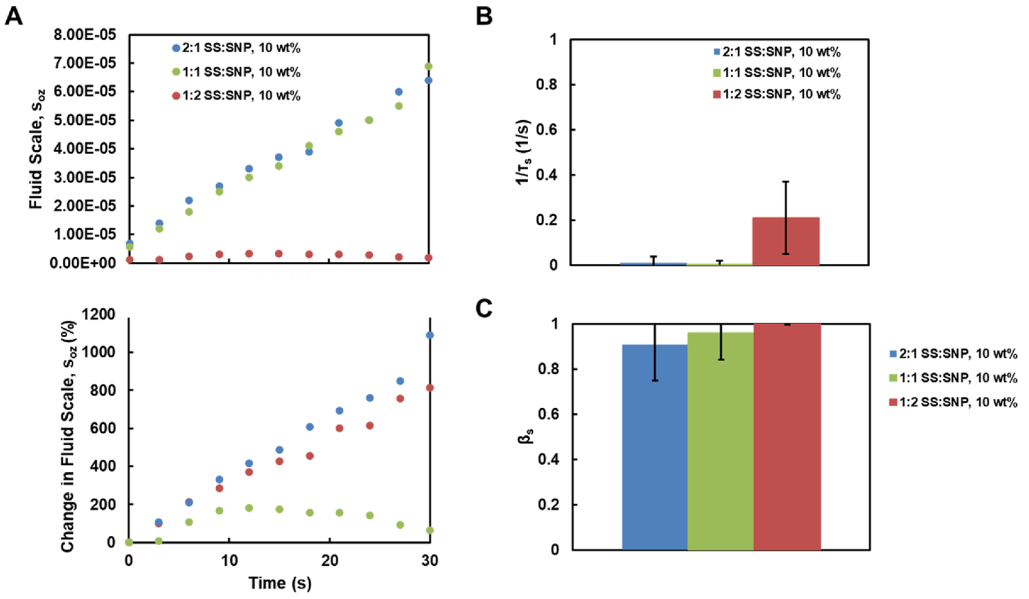

Figure 9. Measured changes in the fluid scale over 30 s of UV exposure ((A) top = absolute values, bottom = percent changes over the irradiation time) and best-fit time constant ($1/\tau_S$, B) and stretch parameter (β_S, C) for heterogeneous SS/SNP hydrogels formed in the beamline (error bars represent ± standard deviation).

internal electrostatic repulsion between the SNPs accounts for the much higher elastic modulus values observed for both (−)SNP- and (+)SNP-based hydrogels (Figure 4). Interestingly, the correlation length also changes significantly less for the charged SNP precursor gels over the photoirradiation period (Supporting Information, Figures S5 and S7), suggesting less changes in the spacing between the SNP structure during photogelation relative to the uncharged precursor nanoparticles; this observation is again consistent with reduced covalent crosslinking and more charge−charge repulsion influencing the network structure of charged SNP hydrogels.

Analysis of the Porod and fluid/Lorentzian exponent trends during photopolymerization for 35 wt % (Supporting Information, Figure S6) and for 25 wt % (Supporting Information, Figure S8) homogeneous hydrogels prepared with charged SNP precursors gives further insight into the SNP responses to photocrosslinking. For both (−)SNP and (+)SNP, the initial fluid exponent is significantly lower than that observed with (0)SNP, consistent with the increase in charge-induced swelling (and thus chain hydration) in the SNPs; however, upon photocrosslinking, the fluid exponent increases significantly in the first few seconds of exposure before slowly decreasing (albeit remaining at a much higher number than that observed prior to photogelation) as crosslinking proceeds. We interpret this result as being related to bringing the charged SNPs closer together during crosslinking, inducing some transient deswelling in the SNPs to maximize the interparticle distance and reduce interparticle repulsion; slow relaxation (and partial reswelling over time) then occurs as the network relaxes to a new equilibrium (crosslinked) state. At the same time, the Porod exponent of the (−)SNP hydrogels remains essentially unchanged during photopolymerization, consistent with the SNPs remaining as discrete particles during the photopolymerization process. The reason for the slight (−25−27%) decrease in the Porod exponent of the (+)SNP gels is less clear but may be related to the significantly smaller initial size and higher propensity for nanoclustering of (+)SNPs in suspension compared to (−)SNP and (0)SNP (Table 1). Thus, unlike the (0)SNP hydrogels in which the SNPs do not repel each other and the vSANS results suggest a degree of SNP swelling as a result of crosslink formation, (+)SNP- and (−)SNP-based hydrogels appear to deswell to some degree to compensate for the interparticle repulsion in the context of the constrained gel volume.

3.3.3. Effect of the Starch Morphology. To assess the impact of mixing starch morphologies within a single hydrogel, Figure 9 shows the measured changes in the fluid scale (Figure 9A) and the values of the best-fit $1/\tau_S$ (Figure 9B) and β_S (Figure 9C) values for heterogeneous starch hydrogels fabricated by varying the ratio of the SS and SNP precursors used to form the hydrogel (10 wt % total concentration in all cases); see Supporting Information, Figure S11 for the corresponding correlation length data.

The evolution of the fluid scale is very similar for the 2:1 SS:SNP 10 wt % and 1:1 SS:SNP 10 wt % hydrogels, with both gels showing nearly linear increases in the fluid scale and virtually no measurable exponential time constant (i.e., negligible $1/\tau$) over the entire duration of the 30 s UV exposure period (consistent with the (0)SNP data, Figures 6A and 7A); in contrast, the magnitude of the fluid scale is consistent with the (0)SS data collected at the same concentration (Figure 8A), with the percentage change in the fluid scale lying between that observed for SS-only and SNP-only hydrogels. Hence, replacing a fraction of the SS with SNP slows down gelation due to the replacement of the larger/more conformationally mobile SS with SNPs (consistent with the bulk gelation data in Table 2) and results in a significantly weaker hydrogel (Figure 4) but ultimately achieves a similar fluid scale on the microscale. While the 1:2 SS:SNP 10 wt % hydrogel has an even slower gelation time (Table 2, as expected by replacing more of the SS with SNPs), the fluid scale trend is completely different in that only a very small increase in the fluid scale was observed over the first 5−7 s of the experiment after which the fluid scale plateaus, leading to a

https://doi.org/10.1021/acs.macromol.2c00874
Macromolecules XXXX, XXX, XXX−XXX

measurable relaxation time (Figure 9B). In this case, the fluid scale trend is very similar in terms of both shape and magnitude to that observed with the charged SNP hydrogels (Figures 6A and 7A). Correspondingly, the 1:2 SS:SNP hydrogel is significantly stiffer than the 1:1 SS:SNP hydrogel (Figure 5). This result suggests that a minor fraction of soluble branched SS may act as both a covalent macromolecular crosslinker as well as a functional steric stabilizer for the major SNP fraction, resulting in the formation of a hydrogel with a lower covalent crosslink density but higher internal inter-nanoparticle repulsion that results in the higher observed modulus values. The stretch parameter does not change significantly within the best-fit error, although the general trend of lower β_S values in SS-rich hydrogels remains consistent.

The changes in the Porod and fluid/Lorentzian exponents for heterogeneous SS:SNP hydrogels also show intermediate values compared to those observed for homogeneous SNP- and SS-based hydrogels (Supporting Information, Figure S12). The Porod exponents decreased slightly by 6 (2:1 SS:SNP 10 wt %), 5 (1:1 SS:SNP 10 wt %), and 14% (1:2 SS:SNP 10 wt %), while the fluid exponents decreased slightly by 3, 0, and 7% during the photocrosslinking process. These small changes are all consistent with the opposing effects of SNPs (fixed Porod exponent, reducing fluid exponent over time) and SS (reducing Porod exponents over time, fixed fluid exponent) on the overall hydrogel properties, resulting in intermediate properties when SNPs and SS are mixed.

To our knowledge, this is the first report on the characterization of time-resolved gelation kinetics driven by UV crosslinking using SANS, a measurement that is uniquely enabled by the vSANS instrument at NIST. Coupling these measurements with *in situ* photorheometry allows for correlation between the microscale (vSANS) and macroscale (rheometry) structure evolution during photocrosslinking. While clear correlations were observed between the bulk and microscale data in many systems (e.g., with regard to the effect of concentration on the hydrogel properties), the differences observed between the mechanics of the hydrogel and the evolution of the fluid scale were strikingly different depending on the charge and morphology of the starch building blocks. We hypothesize that the correlation of the fluid scale to the liquid-to-solid transition enables discrimination between the formation of new crosslinks and differences in the interparticle interactions in the precursor gel suspension that are otherwise challenging to discriminate using different techniques. This approach is particularly valuable for gaining a better fundamental understanding of crosslinking in nanoparticle network hydrogels in which an already internally crosslinked microgel particle is used as one of the building blocks and the distinction between the effects of the intraparticle and interparticle crosslinking via bulk hydrogel measurements is otherwise challenging to explicitly identify. Tracking of the Porod and Lorentzian exponents allows for additional insight into how individual starch starting materials in the network respond to the photogelation process, with crosslinking observed to induce swelling (neutral SNPs), deswelling (charged SNPs), or no changes in the solvation of the constituent starch (neural SS) depending on the morphology of the starch building blocks and whether strong repulsive forces exist between constituent SNP building blocks. Such information is only accessible using SANS given that the length scales analyzed are not accessible using other techniques. We anticipate that similar considerations would also apply in any system in which hydrogel-based nanoscale and/or linear polymer building blocks with defined charge densities are used to form bulk hydrogels, although such extrapolations should be experimentally tested given the somewhat unique small size of SNPs among typically available nanogel-based building blocks.

4. CONCLUSIONS

Tracking the kinetics of the microscale (very small-angle neutron scattering) and macroscale (small-amplitude oscillatory shear rheology) evolution of the photopolymerization of methacrylated soluble (branched) starch and/or starch nanoparticles with varying charges yields key physical insights into the structure−property relationships in such hydrogels. In particular, this strategy enabled the elucidation of three key differences in the bulk versus microscale trends observed: (1) the fluid scale of neutral SNP-based hydrogels continues to increase over time well past the time at which macroscopic gelation was observed, suggesting significant reconformations within the SNP building blocks to drive higher interparticle crosslinking over time in such systems; (2) hydrogels formed based on charged starch nanoparticles exhibited stiffer mechanics but much smaller changes in the fluid scale as a function of time relative to neutral starch nanoparticle-based hydrogels, suggesting that interparticle repulsion is playing a key role in maintaining the bulk rheological properties of these hydrogels; and (3) hydrogels prepared with mixtures of soluble branched starch and starch nanoparticles exhibited highly decoupled changes between the fluid scale and the mechanics depending on whether the soluble starch (higher hydrodynamic diameter and higher conformational mobility) or the starch nanoparticles (smaller hydrodynamic diameter and smaller conformational mobility) represented the major fraction, with the 1:1 ratio unexpectedly resulting in the weakest hydrogel. In addition, charged SNPs deswell during photocrosslinking to compensate for the close charge−charge repulsion between SNPs in the constrained gel volume, while neutral SNPs slightly swell upon crosslinking as the interparticle crosslinks counteract the swelling restrictions imposed by the intraparticle crosslinks. We believe that the approach demonstrated herein is generally applicable to better understand the role of the charge, morphology, and/or size of other types of soft building blocks in forming photocrosslinked hydrogels, informing the rational design of such hydrogels with targeted comprehensive properties.

■ ASSOCIATED CONTENT

Supporting Information

The Supporting Information is available free of charge at https://pubs.acs.org/doi/10.1021/acs.macromol.2c00874.

Quantification of sulfation density via charge titration and elemental analysis, comparison graphs of pregelation viscosity sweep data, dynamic oscillatory rheology measurements tracking modulus development during photocrosslinking, plots of correlation length and corresponding vSANS fitting parameters as a function of time, and all raw vSANS best-fit parameters and parameter error estimates (PDF)

https://doi.org/10.1021/acs.macromol.2c00874
Macromolecules XXXX, XXX, XXX−XXX

AUTHOR INFORMATION

Corresponding Author

Todd Hoare − *Department of Chemical Engineering, McMaster University, Hamilton, Ontario L8S 4L8, Canada;* orcid.org/0000-0002-5698-8463; Email: hoaretr@mcmaster.ca

Authors

Michael J. Majcher − *Department of Chemical Engineering, McMaster University, Hamilton, Ontario L8S 4L8, Canada*

Sebastian Himbert − *Department of Physics & Astronomy, McMaster University, Hamilton, Ontario L8S 4L8, Canada*

Francesco Vito − *Department of Chemical Engineering, McMaster University, Hamilton, Ontario L8S 4L8, Canada*

Matthew A. Campea − *Department of Chemical Engineering, McMaster University, Hamilton, Ontario L8S 4L8, Canada*

Ridhdhi Dave − *Department of Chemical Engineering, McMaster University, Hamilton, Ontario L8S 4L8, Canada*

Grethe Vetergaard Jensen − *NIST Center for Neutron Research, National Institute of Standards and Technology, Gaithersburg, Maryland 20899-6100, United States;* Present Address: Present address: Danish Technological Institute, Tåstrup, Denmark (G.V.J.)

Maikel C. Rheinstadter − *Department of Physics & Astronomy, McMaster University, Hamilton, Ontario L8S 4L8, Canada;* orcid.org/0000-0002-0558-7475

Niels M. B. Smeets − *Department of Chemical Engineering, McMaster University, Hamilton, Ontario L8S 4L8, Canada*

Complete contact information is available at: https://pubs.acs.org/10.1021/acs.macromol.2c00874

Funding

The Natural Sciences and Engineering Research Council of Canada (NSERC, Strategic Project Grant 463327-14) is gratefully acknowledged for funding this work. This work utilized facilities supported in part by the National Science Foundation under Agreement No. DMR-0944772. We acknowledge support of the National Institute of Standards and Technology, US Department of Commerce, in providing the neutron facilities used in this work. Use of facilities provided by McMaster's Biointerfaces Institute and EcoSynthetix, Inc. is also gratefully acknowledged.

Notes

Certain commercial equipment, instruments, or materials are identified in this paper to foster understanding. Such identification does not imply recommendation or endorsement by the National Institute of Standards and Technology, nor does it imply that the materials and equipment identified are necessarily the best available for the purpose.

The authors declare no competing financial interest.

ACKNOWLEDGMENTS

We acknowledge support of the National Institute of Standards and Technology, US Department of Commerce, in providing the neutron research facilities used in this work. The authors would like to specifically acknowledge Markus Blueul, Kenneth A. Rubinson, and Juscelino Leao at the National Institute of Standards and Technology for their assistance in setting up the custom vSANS equipment used to irradiate the samples next to the beamline during our experiment. The authors would also like to thank McMaster University's NMR facility for assistance in acquiring the reported NMR data. Lastly, Dr. Jean Duhamel is acknowledged for his useful discussions on the analysis of the vSANS data. Access to NGA-NSE and the NGB30-SANS was provided by the Center for High Resolution Neutron Scattering, a partnership between the National Institute of Standards and Technology and the National Science Foundation under Agreement No. DMR-2010792.

REFERENCES

(1) Hoare, T. R.; Kohane, D. S. Hydrogels in drug delivery: Progress and challenges. *Polymer* **2008**, *49*, 1993−2007.

(2) Rabe, M.; Verdes, D.; Seeger, S. Understanding protein adsorption phenomena at solid surfaces. *Adv. Colloid Interface Sci.* **2011**, *162*, 87−106.

(3) Horbett, T. A.; Brash, J. L. Proteins at Interfaces: Current Issues and Future Prospects. 1987, 1−33, DOI: 10.1021/bk-1987-0343.ch001.

(4) Campuzano, S.; Pedrero, M.; Yáñez-Sedeño, P.; Pingarrón, J. Antifouling (Bio)materials for electrochemical (bio)sensing. *Int. J. Mol. Sci.* **2019**, *20*, 423.

(5) Liu, N.; Xu, Z.; Morrin, A.; Luo, X. Low fouling strategies for electrochemical biosensors targeting disease biomarkers. *Anal. Methods* **2019**, *11*, 702−711.

(6) Deng, X.; Korogiannaki, M.; Rastegari, B.; Zhang, J.; Chen, M.; Fu, Q.; Sheardown, H.; Filipe, C. D. M.; Hoare, T. "click" Chemistry-Tethered Hyaluronic Acid-Based Contact Lens Coatings Improve Lens Wettability and Lower Protein Adsorption. *ACS Appl. Mater. Interfaces* **2016**, *8*, 22064.

(7) Shimoda, A.; ichi Sawada, S.; Kano, A.; Maruyama, A.; Moquin, A.; Winnik, F. M.; Akiyoshi, K. Dual crosslinked hydrogel nanoparticles by nanogel bottom-up method for sustained-release delivery. *Colloids Surf., B* **2012**, *99*, 38−44.

(8) Smeets, N. M. B.; Bakaic, E.; Patenaude, M.; Hoare, T. Injectable poly(oligoethylene glycol methacrylate)-based hydrogels with tunable phase transition behaviours: Physicochemical and biological responses. *Acta Biomater.* **2014**, *10*, 4143−4155.

(9) Wang, J.; Sun, H.; Li, J.; Dong, D.; Zhang, Y.; Yao, F. Ionic starch-based hydrogels for the prevention of nonspecific protein adsorption. *Carbohydr. Polym.* **2015**, *117*, 384−391.

(10) Meng, H.; Cheng, Q.; Wang, H.; Li, C. Improving anti-protein-fouling property of polyacrylonitrile ultrafiltration membrane by grafting sulfobetaine zwitterions. *J. Chem.* **2014**, *2014*, 1.

(11) Deng, X.; Smeets, N. M. B.; Sicard, C.; Wang, J.; Brennan, J. D.; Filipe, C. D. M.; Hoare, T. Poly(oligoethylene glycol methacrylate) dip-coating: Turning cellulose paper into a protein-repellent platform for biosensors. *J. Am. Chem. Soc.* **2014**, *136*, 12852−12855.

(12) Russell, S. M.; Carta, G. Multicomponent protein adsorption in supported cationic polyacrylamide hydrogels. *AIChE J.* **2005**, *51*, 2469−2480.

(13) Majcher, M. J.; Hoare, T. Hydrogel Synthesis and Design. *Functional Biopolymers*; Springer International Publishing 2019, DOI: 10.1007/978-3-319-95990-0_9.

(14) Ahmed, E. M. Hydrogel: Preparation, characterization, and applications: A review. *J. Adv. Res.* **2015**, *6*, 105−121.

(15) Pekař, M. Hydrogels with micellar hydrophobic (nano)-domains. *Front. Mater.* **2015**, *1*, 1−14.

(16) Huang, Y.; Wang, Y.; Sun, L.; Agrawal, R.; Zhang, M. Sundew adhesive: A naturally occurring hydrogel. *J. R. Soc., Interface* **2015**, *12*, 20150226.

(17) Campea, M. A.; Majcher, M. J.; Lofts, A.; Hoare, T. A Review of Design and Fabrication Methods for Nanoparticle Network Hydrogels for Biomedical, Environmental, and Industrial Applications. *Adv. Funct. Mater.* **2021**, 2102355.

(18) Majcher, M. J.; McInnis, C. L.; Himbert, S.; Alsop, R. J.; Kinio, D.; Bleuel, M.; Rheinstädter, M. C.; Smeets, N. M. B.; Hoare, T. Photopolymerized Starchstarch Nanoparticle (SNP) network hydrogels. *Carbohydr. Polym.* **2020**, *236*, No. 115998.

(19) Rochas, C.; Geissler, E. Measurement of dynamic light scattering intensity in gels. *Macromolecules* **2014**, *47*, 8012−8017.

(20) Bussche, E. V.; De Deene, Y.; Dubruel, P.; Vergote, K.; Schacht, E.; De Wagter, C. The use of static light scattering for the structure analysis of radiosensitive polymer gels: a literature survey. *J. Phys. Conf. Ser.* **2004**, *3*, 180−183.
(21) Gomes, C.; Dias, R. C.; Costa, M. R. P. Static light scattering monitoring and kinetic modeling of polyacrylamide hydrogel synthesis. *Processes* **2019**, *7*, 1−25.
(22) Waters, D. J.; Engberg, K.; Parke-Houben, R.; Hartmann, L.; Ta, C. N.; Toney, M. F.; Frank, C. W. Poly(ethylene, Morphology of Photopolymerized End-linked Scattering, glycol) Hydrogels by Small Angle X-ray. *Macromolecules* **2010**, *43*, 6861−6870.
(23) Nack, A.; Seifert, J.; Passow, C.; Wagner, J. Hindered nematic alignment of hematite spindles in poly(N-isopropylacrylamide) hydrogels: A small-angle X-ray scattering and rheology study: A. *J. Appl. Crystallogr.* **2018**, *51*, 87−96.
(24) Tripathi, A.; Parsons, G. N.; Khan, S. A.; Rojas, O. J. Synthesis of organic aerogels with tailorable morphology and strength by controlled solvent swelling following Hansen solubility. *Sci. Rep.* **2018**, *8*, 2106.
(25) Pouliot, R. A.; Young, B. M.; Link, P. A.; Park, H. E.; Kahn, A. R.; Shankar, K.; Schneck, M. B.; Weiss, D. J.; Heise, R. L. Porcine Lung-Derived Extracellular Matrix Hydrogel Properties Are Dependent on Pepsin Digestion Time. *Tissue Eng., Part C* **2020**, *26*, 332−346.
(26) Trudicova, M.; Smilek, J.; Kalina, M.; Smilkova, M.; Adamkova, K.; Hrubanova, K.; Krzyzanek, V.; Sedlacek, P. Multiscale experimental evaluation of agarose-based semi-interpenetrating polymer network hydrogels as materials with tunable rheological and transport performance. *Polymer* **2020**, *12*, 1−27.
(27) Szepes, A.; Makai, Z.; Blümer, C.; Mäder, K.; Kása, P., Jr.; Szabó-Révész, P. Characterization and drug delivery behaviour of starch-based hydrogels prepared via isostatic ultrahigh pressure. *Carbohydr. Polym.* **2008**, *72*, 571−578.
(28) Roy, A.; Bajpai, A. K.; Bajpai, J. Designing swellable beads of alginate and gelatin for controlled release of pesticide (cypermethrin). *J. Macromol. Sci., Part A: Pure Appl. Chem.* **2009**, *46*, 847−859.
(29) Tian, J.; Seery, T. A. P.; Weiss, R. A. Physically cross-linked alkylacrylamide hydrogels: Phase behavior and microstructure. *Macromolecules* **2004**, *37*, 9994−10000.
(30) Hammouda, B.; Ho, D. L. Insight into Chain Dimensions in PEO/Water Solutions. *J. Polym. Sci., Part B: Polym. Phys.* **2007**, *45*, 2196−2200.
(31) Sanson, N.; Rieger, J. Synthesis of nanogels/microgels by conventional and controlled radical crosslinking copolymerization. *Polym. Chem.* **2010**, *1*, 965−977.
(32) Smeets, N. M. B.; Bakaic, E.; Yavitt, F. M.; Yang, F.-C.; Rheinstädter, M. C.; Hoare, T. Probing the internal morphology of injectable poly(oligoethylene glycol methacrylate) hydrogels by light and small-angle neutron scattering. *Macromolecules* **2014**, *47*, 6017−6027.
(33) Shibayama, M. Small-angle neutron scattering on polymer gels: Phase behavior, inhomogeneities and deformation mechanisms. *Polym. J.* **2011**, *43*, 18−34.
(34) Jamard, M.; Hoare, T.; Sheardown, H. Nanogels of methylcellulose hydrophobized with N-tert-butylacrylamide for ocular drug delivery. *Drug Deliv. Transl. Res.* **2016**, *6*, 648−659.
(35) Yadav, H. K. S.; Anwar, N.; Halabi, A.; Alsalloum, G. A. Nanogels as Novel Drug Delivery Systems - A Review Properties of Nanogels Keywords : Introduction Advantages of Nanogels. *Insight Pharma Res.* **2017**, *1*, 1−8. http://www.imedpub.com/articles/nanogels-as-novel-drug-delivery-systems–a-review.php?aid=18950
(36) Hoare, T.; Young, S.; Lawlor, M. W.; Kohane, D. S. Thermoresponsive nanogels for prolonged duration local anesthesia. *Acta Biomater.* **2012**, *8*, 3596−3605.
(37) Huibers, P. D. T.; Bromberg, L. E.; Robinson, B. H.; Hatton, T. A. Reversible gelation in semidilute aqueous solutions of associative polymers: a small-angle neutron scattering study. *Macromolecules* **1999**, *32*, 4889−4894.
(38) Koh, A. Y. C.; Saunders, B. R. Small-angle neutron scattering study of temperature-induced emulsion gelation: The role of sticky microgel particles. *Langmuir* **2005**, *21*, 6734−6741.
(39) Chodankar, S.; Aswal, V. K.; Kohlbrecher, J.; Vavrin, R.; Wagh, A. G. Small-angle neutron scattering study of structure and kinetics of temperature-induced protein gelation. *Phys. Rev. E* **2009**, *79*, 1−7.
(40) Hashimoto, K.; Fujii, K.; Nishi, K.; Shibayama, M. Ion Gel Network Formation in an Ionic Liquid Studied by Time-Resolved Small-Angle Neutron Scattering. *J. Phys. Chem. B.* **2018**, *122*, 9419−9424.
(41) Barbier, V.; Hervé, M.; Sudor, J.; Brulet, A.; Hourdet, D.; Viovy, J. L. Thermally induced gelation of poly(acrylamide) grafted with poly(N-isopropylacrylamide): A small-angle neutron scattering study. *Macromolecules* **2004**, *37*, 5682−5691.
(42) Butler, B. D.; Muzny, C. D.; Hanley, H. J. M. Scaling of small-angle neutron scattering intensities from gelling colloidal silica. *Int. J. Thermophys.* **1999**, *20*, 35−43.
(43) Shibayama, M.; Kawada, H.; Kume, T.; Matsunaga, T.; Iwai, H.; Sano, T.; Osaka, N.; Miyazaki, S.; Okabe, S.; Endo, H. In situ small-angle neutron scattering and rheological measurements of shear-induced gelation. *J. Chem. Phys.* **2007**, *127*, 144507.
(44) Kline, S. R. Reduction and analysis of SANS and USANS data using IGOR Pro. *J. Appl. Crystallogr.* **2006**, *39*, 895−900.
(45) Wang, Q.; Gu, Z.; Jamal, S.; Detamore, M. S.; Berkland, C. Hybrid hydroxyapatite nanoparticle colloidal gels are injectable fillers for bone tissue engineering. *Tissue Eng Part A.* **2013**, *19*, 2586−2593.
(46) Wang, Q.; Jamal, S.; Detamore, M. S.; Berkland, C. PLGA-chitosan/PLGA-alginate nanoparticle blends as biodegradable colloidal gels for seeding human umbilical cord mesenchymal stem cells. *J. Biomed. Mater. Res., Part A* **2011**, *96A*, 520−527.
(47) Gomez, E. W.; Clack, N. G.; Wu, H. J.; Groves, J. T. Like-charge interactions between colloidal particles are asymmetric with respect to sign. *Soft Matter* **2009**, *5*, 1931−1936.
(48) Giezen, F.E.; Jongboom, R.O.J.; Feil, H.; Gotlieb, K.F.; Boersma, A. *Process for producing biopolymer nanoparticles*, PCT Int. Appl. (2000) 17 pp.
(49) Takano, R.; Nagai, T.; Wu, X.; Xu, X. Y.; Huy, N. T.; Kamei, K.; Hara, S. Sulfation of polysaccharides using monomethyl sulfate. *J. Carbohydr. Chem.* **2000**, *19*, 1185−1190.
(50) Criag, S. A. S.; Maningat, C. C.; Seib, P. A.; Hoseney, R. C. Starch paste clarity. *Cereal Chem.* **1989**, *66*, 173−182.
(51) Mousseau, F.; Vitorazi, L.; Herrmann, L.; Mornet, S.; Berret, J. F. Polyelectrolyte assisted charge titration spectrometry: Applications to latex and oxide nanoparticles. *J. Colloid Interface Sci.* **2016**, *475*, 36−45.
(52) Sakurada, O.; Kato, Y.; Kito, N.; Kameyama, K.; Hattori, T.; Hashiba, M. Colloidal Titration of Aqueous Zirconium Solutions with Poly(vinyl sulfate) by Potentiometric Endpoint Detection Using a Toluidine Blue Selective Electrode. *Anal. Sci.* **2004**, *20*, 311−314.
(53) Duffy, J. *Measuring the rheology of polymer solutions*; Malvern Instruments Ltd. (2015) 1−13. www.malvern.com/contact.
(54) Chen, T. UV Curing Analysis Using A Rheometer. *TA Instrum.* n.d. 2−6
(55) Barker, J.; Moyer, J.; Kline, S.; Jensen, G.; Cook, J.; Gagnon, C.; Kelley, E.; Chabot, J. P.; Maliszewskyj, N.; Parikh, C.; Chen, W.; Murphy, R. P.; Glinka, C. The very small angle neutron scattering instrument at the National Institute of Standards and Technology. *J. Appl. Crystallogr.* **2022**, *55*, 271−283.
(56) Norisuye, T.; Masui, N.; Kida, Y.; Ikuta, D.; Kokufuta, E.; Ito, S.; Panyukov, S.; Shibayama, M. Small angle neutron scattering studies on structural inhomogeneities in polymer gels: irradiation cross-linked gels vs chemically cross-linked gels. *Polymer* **2002**, *43*, 5289−5297.
(57) Hammouda, B.; Ho, D. L.; Kline, S. Insight into clustering in poly(ethylene oxide) solutions. *Macromolecules* **2004**, *37*, 6932−6937.
(58) Hammouda, B. *Scattering from Fractal Systems*. In Probing Nanoscale Structures, SANS Toolbox; Natl. Inst. Stand. Technol. (2004). https://www.ncnr.nist.gov/staff/hammouda/the_sans_toolbox.pdf.

https://doi.org/10.1021/acs.macromol.2c00874
Macromolecules XXXX, XXX, XXX−XXX

(59) Gilbert, T.; Alsop, R. J.; Babi, M.; Moran-Mirabal, J.; Rheinstädter, M. C.; Hoare, T. Nanostructure of Fully Injectable Hydrazone-Thiosuccinimide Interpenetrating Polymer Network Hydrogels Assessed by Small-Angle Neutron Scattering and dSTORM Single-Molecule Fluorescence Microscopy. *ACS Appl. Mater. Interfaces* **2017**, *9*, 42179−42191.
(60) Górska, K.; Horzela, A.; Penson, K. A.; Dattoli, G.; Duchamp, G. H. E. The stretched exponential behavior and its underlying dynamics. The phenomenological approach. *Fract. Calc. Appl. Anal.* **2017**, *20*, 260−283.
(61) Berry, G. C.; Plazek, D. J. On the use of stretched-exponential functions for both linear viscoelastic creep and stress relaxation. *Rheol. Acta* **1997**, *36*, 320−329.
(62) Toppozini, L.; Roosen-Runge, F.; Bewley, R. I.; Dalgliesh, R. M.; Perring, T.; Seydel, T.; Glyde, H. R.; Sakai, V. G.; Rheinstädter, M. C. Anomalous and anisotropic nanoscale diffusion of hydration water molecules in fluid lipid membranes. *Soft Matter* **2015**, *11*, 8354−8371.
(63) De Gennes, P. *Pierre-giles De Gennes - Scaling concepts in polymer physics* (1979, Cornell University Press), (1979) 324. https://www.eng.uc.edu/~beaucag/Classes/Properties/Books/Pierre-giles%20De%20Gennes%20-%20Scaling%20concepts%20in%20polymer%20physics-Cornell%20University%20Press%20(1979).pdf De Gennes - Scaling concepts in polymer physics-Cornell University Press (1979).pdf.
(64) Saffer, E. M.; Lackey, M. A.; Griffin, D. M.; Kishore, S.; Tew, G. N.; Bhatia, S. R. SANS Study of Highly Resilient Poly(ethylene glycol) Hydrogels. *Soft Matter* **2014**, *10*, 1905−1916.
(65) Le, D. H.; Pham, C. K.; Nguyen, T. T. T.; Bui, T. T. Parameter extraction and optimization using Levenberg-Marquardt algorithm, 2012 4th Int. *Conf. Commun. Electron;* ICCE 2012, *2012*, 434−437, DOI: 10.1109/CCE.2012.6315945.
(66) Finsterle, S.; Kowalsky, M. B. A truncated Levenberg-Marquardt algorithm for the calibration of highly parameterized nonlinear models. *Comput. Geosci.* **2011**, *37*, 731−738.
(67) Chamberlain, E. K.; Rao, M. A.; Cohen, C. Shear thinning and antithixotropic behavior of a heated cross-linked waxy maize starch dispersion. *Int. J. Food Prop.* **1999**, *2*, 63−77.
(68) Majcher, M. J.; Babar, A.; Lofts, A.; Leung, A.; Li, X.; Abu-Hijleh, F.; Smeets, N. M. B.; Mishra, R. K.; Hoare, T. In situ-gelling starch nanoparticle (SNP)/O-carboxymethyl chitosan (CMCh) nanoparticle network hydrogels for the intranasal delivery of an antipsychotic peptide. *J. Controlled Release* **2021**, *330*, 738−752.

https://doi.org/10.1021/acs.macromol.2c00874
Macromolecules XXXX, XXX, XXX−XXX